JOURNAL OF THE BALKAN GEOPHYSICAL SOCIETY, Vol. 4, No 4, November 2001, p. 69-90, 14 figs.

Effect of earth structure and source time function on inversion of single-station regional surface waves for rupture mechanism and focal depth

Özcan Çakir and Murat Erduran

Department of Geophysics, Black Sea Technical University, 61080, Trabzon, Turkey

(Received 6 April 2000; accepted 15 January 2001)

***Abstract**: A single-station inversion using regional surface waves is tested to determine the rupture mechanism and the focal depth of an earthquake in a more like statistical manner throughout both synthetic seismograms and the actual records. The method works efficiently if the underground velocity structure and the source time function are chosen reasonably correctly. The Love-wave observed group velocities, which are affected least by the source phase shift, might be effectively used to predict the velocity structure. The minimum wave-period of surface waves used in the inversion is an important factor that significantly affects the stability of the method. It should be chosen slightly greater than the minimum of the observed Love-wave periods. The selected source time function should not have significant amount of time shift (e.g. ± 2 s) relative to the actual one. Otherwise, the method easily breaks down. An impulse or a simple triangular pulse properly located in time generally suffices. Synthetic seismogram modeling at the end of the inversion process should be used to check the validity of the model parameters. There is a trade-off between small and large wave-periods. Large periods guarantee stability in the solution while the small ones are necessary to increase the precision. The user of the method should be careful in handling this delicacy between stability and precision.*

***Key words**: Surface Waves, Rupture Mechanism, Focal Depth, Source Time Function, Single-Station Inversion.*

INTRODUCTION

Single-station regional Rayleigh and Love surface waves recorded in the three-component have been utilized for the determination of rupture mechanism and focal depth (e.g. Mendiguren, 1977; Giardini *et al.*,, 1993). An earthquake recording results from a three-fold convolution process, in which the earthquake source function and the impulse response of the earth structure and of the recording instrument are involved (e.g. see Sileny *et al.*, 1992; Panza *et al.*, 1993). The model parameters of this convolution should be known *a priori* in order to apply an efficient analysis about the source characteristics using surface waves. The impulse response of the recording instrument is usually assumed known and not discussed here. The model for the earth structure usually consists of *n* parallel and homogeneous layers overlying a half-space, in which the wave propagation can be described using the normal mode theory (Abo-Zena, 1979; Chen, 1993). The source properties can be parameterised in three parts: source time function (STF), rupture mechanism (MECH) and focal depth. In case that the source time function and the earth structure accurately is known, it is possible to develop an iterative method for the determination of focal depth and also a linear least-square inversion technique for rupture mechanism determination (see Jimenez *et al.*, 1989). The main target of this study is to explore the impact when the source time function and the earth structure are only approximately known.

The surface wave-spectra are a function of several parameters in a non-linear fashion and in fact, a non-linear inversion technique has to be employed to obtain these parameters. However, it is possible to avoid the non-linearity assuming that some of the parameters are known, at least approximately and reduce the problem into a linear case (see Sileny *et al.*, 1992; Panza *et al.*, 1993). In such an approach, the source time function and the earth structure should be known reasonably well. In the following, we show how accurately the rupture mechanism and the focal depth can be recovered from a three-component surface wave recording. We will simulate the surface wave propagation with numerical calculations so that, in case of applications to the real data, the necessary precautions can be taken beforehand. Since we are interested in moderate-size earthquakes only, we assume point-source (double-couple) approximation in our calculations. We restrict our analysis to the regional

surface waves having crustal focal depths. At epicentral distances greater than maximum considered here (4800 km) and at focal depths deeper than the crustal range, the presented analysis may need some revisions.

We will apply the current method to two regional earthquake recordings in that we check the efficiency of the inversion process in the presence of standard noise accompanied by the 3-D heterogeneity in the earth structure that is not considered throughout synthetic calculations. Inverted focal mechanisms in this study are compared to the ones obtained by different seismological institutions.

TEST MODELS AND SOURCE TIME FUNCTIONS

We have numerically simulated the surface wave propagation at the epicentral distances of 300, 600, 1200, 2400 and 4800 km. Dominant surface wave periods increase with epicentral distance and long periods have deep penetration into the earth. Surface waves at the selected maximum distance (4800 km) are able to sample the significant portion of the upper-mantle structure. We have arranged the maximum depth of the test models to extend up to the 700 km depth, which is sufficient for the purpose of the current work.

In Figure 1, we show the depth distribution of the model parameters (i.e. layer thickness, P and S velocities and density). The test models are referenced as Model 1 and Model 2. Model 1 is used to represent a typical earth structure and is equivalent to the most recent models of the real earth in this depth range (Anderson, 1989; Lay and Wallace, 1995). It includes a typical crust with a thickness of 35 km. A thin velocity reversal at a depth of about 150 km, which is identified as the low velocity zone (LVZ), underlying a high velocity seismic LID with a thickness of around 100 km is also present. The two major velocity discontinuities at depths of about 400 and 660 km are also present in the upper mantle.

A second model called Model 2 is also presented in Figure 1. We will use it as an approximation to Model 1, assuming that Model 1 is the structure along which the surface wave propagation actually takes place and Model 2 is assumed to “erroneously” replace Model 1 in the inversion process. It is seen in Figure 1 that the crustal thickness in Model 2 (45 km) is greater than the one in Model 1 (35 km) and also velocities in the crust are somewhat different for each model. The LVZ in the upper mantle is only slightly present in Model 2. It is seen that Model 2 does not feature the above-mentioned 400 and 660 km discontinuities and has a usual velocity increase with depth. We will examine later in the study whether the difference between these models has significant effect on the solution of surface waves for rupture mechanism and focal depth.

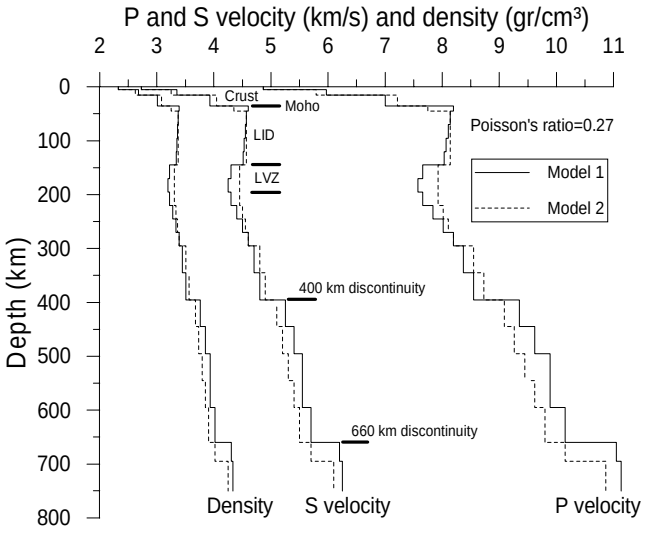

FIG. 1. Crustal and upper-mantle structures utilized in the current study are shown. Model 1 is used to represent surface wave propagation in the real earth. Model 2 approximately represents Model 1 in the inversion of source characteristics.

Source time function is the other parameter that its effect on the inversion scheme will be tested. We have selected three source time functions (STF1, STF2 and STF3) as illustrated by the solid lines in Figure 2. They cover a range of both simple and complex rupture events and represent the typical source time functions usually reported in the literature (e.g. Di Bona and Boatwright, 1991; Taymaz *et al.*, 1991; Hartzell *et al.*, 1994; Ayele and Arvidsson, 1998). We will produce synthetic seismograms using each source time function shown in Figure 2, and replace the “true” source time function with another one, in order to see the effect of this faulty selection on the solution of rupture mechanism and focal depth.

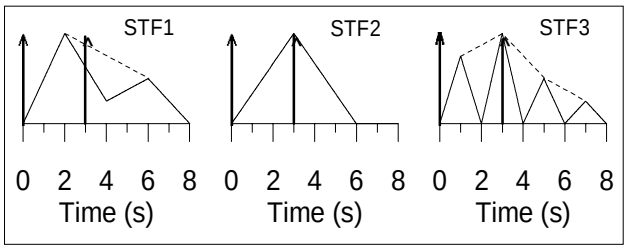

FIG. 2. Selected source time functions (STF) to represent the temporal variation of moment release. See text for more explanation.

NORMAL MODES AND SYNTHETIC SEISMOGRAMS

We have included the fundamental and also up to the fourth higher mode in the analysis. In general, higher mode contribution to the observed surface waveforms decreases with the increase of the mode number, and in fact, a usual surface wave recording exhibits mostly the fundamental mode energy and perhaps a few higher mode contributions.

In Figure 3, we show dispersion curves (the phase and the group velocities) of Rayleigh and Love surface waves for Model 1 and 2 from period of 2 to 200 s. The phase and the group velocities are displayed by separate figures and a different line pattern is used for Model 1 and 2 (Fig. 3). It is seen that the difference between Rayleigh and Love waves is mainly observed on the fundamental dispersion curve, and the higher modes for both waves closely resemble each other.

In seismic wave propagation, low wave-periods exhibit greater sensitivity to the fine details in velocity structure, e.g. velocity discontinuities and depth to the Moho, whereas large wave-periods travel in the medium mostly averaging throughout the structural features. Low periods in surface waves mostly occur in the higher modes. The fundamental mode also accommodates some low periods, but their penetration depth is much shallower than a higher mode at certain period (see Chen, 1993).

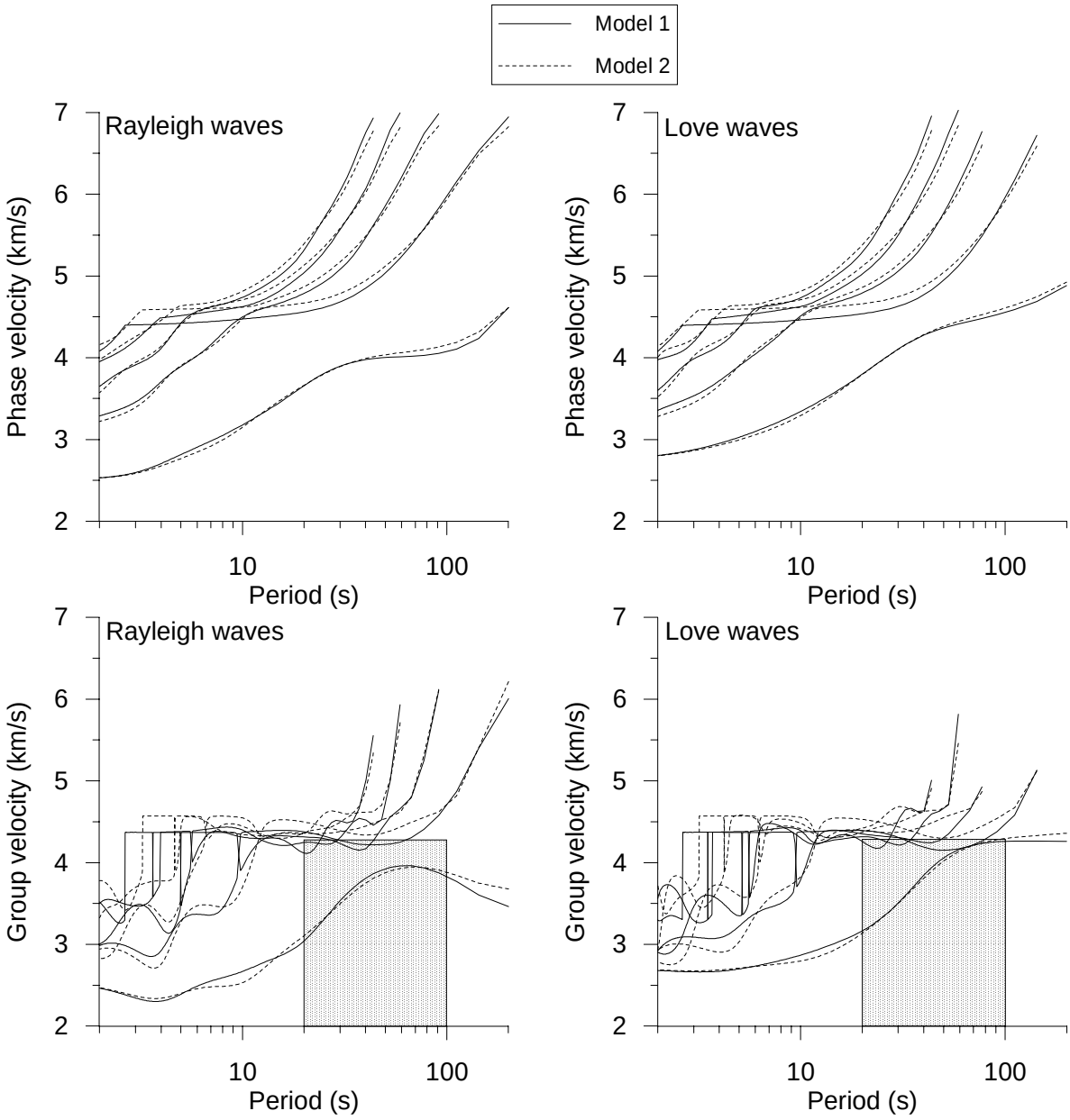

FIG. 3. Phase and group velocities of Rayleigh and Love waves computed for Model 1 and Model 2 given in Fig. 1. Fundamental and up to the fourth higher mode dispersion curves are shown. Free surface amplitudes corresponding to the shaded rectangular box from 20 to 100 s are used for the determination of source characteristics.

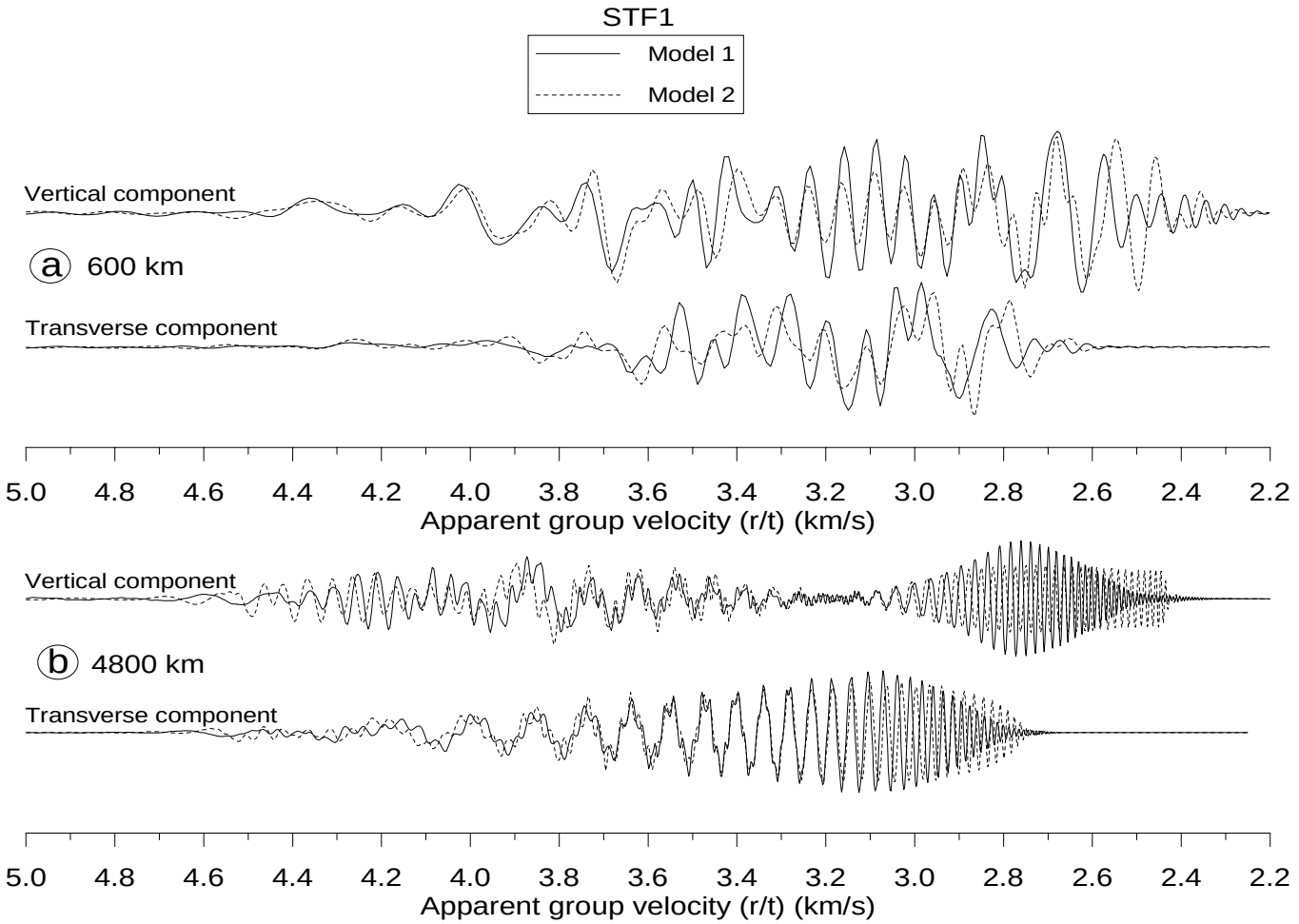

FIG. 4. Surface wave synthetic seismograms computed at a) 600 km epicentral distance and b) 4800 km epicentral distance. Rayleigh waves in the vertical component and Love waves in the transverse component are shown. Apparent group velocity is obtained from the epicentral distance divided by the travel time.

As we will show later, we should avoid low period amplitudes since they will be sensitive to a possible error in the presumed earth structure. We will try to avoid the uncertainty which may come from the structural error, but at the same time try to keep the important information about rupture mechanism and focal depth, provided by low periods, as much as possible.

In Figure 3, one observes that higher mode dispersion curves around 4.5 km/s velocity are closely packed and become near flat, which is called the stationary phase propagation (see Panza *et al.,* 1972; Kausel *et al.,* 1977; Mantovani *et al.,* 1977). This occurs because higher mode surface waves are trapped at depths of the LID and the LVZ combined (see Fig. 1), producing significant low period amplitudes at the free surface. It is also seen that this stationary phase extends up to large periods as well. These wavelengths start penetrating even below the LVZ with the increase of period and have gradually less significant amplitudes at the free surface, as will be shown in the synthetic seismograms section. In addition, higher modes with phase velocity greater than about 4.5 km/s have no significant energy contribution to the free surface amplitudes, either. They become significant when the earthquake focal depth is very deep. As a matter of fact, they propagate deep in the mantle and have no effect on the analysis performed in this work.

There is another higher mode group below the 4.5 km/s stationary phase in Figure 3, which are mainly crustal surface waves penetrating deeper into the LID with increasing wavelength. Their contribution to the free surface amplitudes is significant at particularly small epicentral distances. In this group, there is another stationary phase featuring around 3.5 km/s group velocity, which is called Lg phase (see Kennett, 1989). Lg phase is able to propagate long ranges along with particularly homogeneous crustal structure having high quality factors (Q) (Koch and Stump, 1995; Shi *et al.,* 1996). It is seen in Figure 3 that Lg phase and the other crustal higher modes have the period range below 10 s. As will be shown later in the study, we will not use surface waves below 20 s period for the solution of rupture mechanism and focal depth. Lg phase and the

other crustal higher modes have no importance in the current study and will be avoided.

Now let us compare the dispersion curves for Model 1 and 2 in Figure 3. We are looking for a period range in that they look similar and replace one another. It is seen that the difference in higher modes is significant for all the period range and becomes more significant at particularly low periods. Notice that the fundamental mode in the period range from about 20 to 100 s appear the most appropriate part that we are looking for. The higher modes below 20 s period are most sensitive to the difference between Model 1 and 2 and need be avoided since these either crustal or upper mantle below 20 s period produce significant free surface amplitudes. On the other hand, the higher mode dispersion curves for both models in the period range from 20 to 100 s look quite dissimilar. In fact, this causes no problem since, as stated above, the higher modes in this period range result in no significant free surface amplitudes.

We have calculated synthetic seismograms at 600 and 4800 km epicentral distances to show the modal distribution of the free surface amplitudes (Fig. 4). Synthetics for Model 1 and 2 were superimposed on each other with a different line pattern. In the calculations, it was assumed that a strike-slip fault with strike = 180^o, dip = 90^o and rake = 180^o was placed at 20 km focal depth and that seismic waves were observed at 70^o azimuth from the station. STF1 in Figure 2 was utilized to represent the temporal distribution of moment release at the source. It is seen that the surface waves at 600 km (Fig. 4a) travel mostly in the crust having the largest apparent group velocity around 4.1 km/s. Both signals for Model 1 and 2 at 600 km show the most appropriate resemblance in the range from about 3.3 to 2.6 km/s in Rayleigh waves and from about 3.3 to 2.8 km/s in Love waves. In these velocity ranges, some higher mode interference occurs, but they pose no problem since their effect is reduced with the elimination of low periods. It is also noted that the usable maximum surface wave period goes as high as about 30 s, because of the low epicentral distance.

In Figure 4b, the synthetic signals at 4800 km are shown. The maximum apparent group velocity goes as high as 4.8 km/s, which means that surface waves below the LVZ (see Fig. 1 and Fig. 3) do not contribute much energy at even this distance. It is again seen in Figure 4b that the signal resemblance from about 3.8 to 3.0 km/s in Rayleigh waves and from about 4.0 to 3.1 km/s in Love waves is the most appropriate part that can be used in the retrieval of rupture mechanism and focal depth. It is noted that low periods in particularly the fundamental mode should be avoided and that the maximum available period at 4800 km is around 80 s.

In summary, one is left with the dispersion window given in Figure 3 by a shaded rectangular box from period of 20 to 100 s, from which a surface wave solution of the source regime in the presumed epicentral distance range can be obtained. It is noted that for epicentral distances less than, for example, the presumed minimum here (300 km) the need for a correct crustal structure in the solution is increased, since then the window in Figure 3 narrows down to very low periods. In addition, the fundamental mode beyond period of 100 s shows some inconvenience (Fig. 3). This results from the velocity difference between Model 1 and 2 in the LVZ (see Fig. 1) and actually poses no problem since the free surface amplitudes from this depth do not alter our results. However, at epicentral distances such as greater than, for example, 5000 km and for focal depths below the crustal structure (i.e. subduction zones), the need for a correct velocity profile around the LVZ increases. It should be noted in Figure 3 that the higher modes below even 100 s period sample the structure as deep as 700 km, as can be seen from the difference between the dispersion curves for Model 1 and 2 (compare Figs. 1 and 3). However, the fundamental mode at even 200 s period samples the structure as deep as about 350 km (compare Figs. 1 and 3).

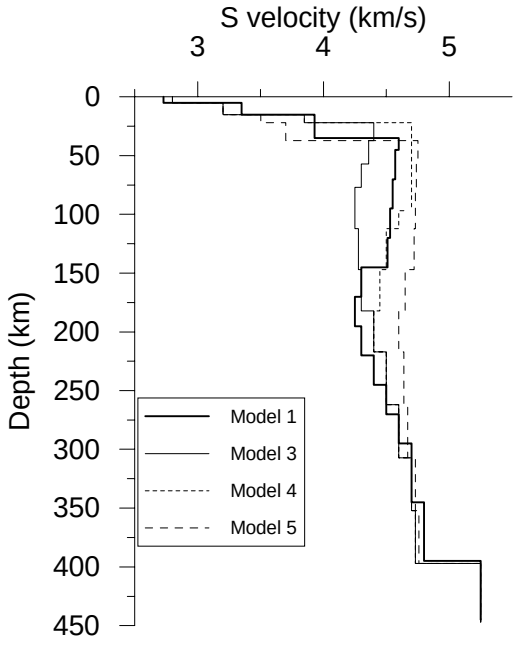

FIG. 5. Various crustal and upper-mantle velocity structures tested in normal mode and synthetic seismogram calculations are shown. See text for more explanation.

It should be noted that the deviation of Model 2 from Model 1 is effectively small (see Fig. 1) which results in the convergence of the fundamental modes of

two models as explained above. In order to test the impact of various erroneous models in place of the correct one (Model 1), we have examined three other models as shown in Figure 5 (Model 3, 4 and 5), in place of Model 2 in Fig. 1. The new models represent some different tectonic provinces (see Lay and Wallace, 1995; Dufumier and Cara, 1995), which are characterized by various crustal-thickness and upper-mantle velocity-depth profile. In the epicentral distance range currently implemented, we have seen throughout several test calculations that seismic velocities below the upper mantle zone have little effect on our analysis. Therefore, we let the new models deviate from the true one above depth of 450 km only as shown in Figure 5. In the models, it is seen that velocity at the Moho discontinuity and depth to the LVZ below the LID vary considerably from one model to the other and that all the test models feature the LVZ to various degree.

We have performed normal mode calculations for each model as shown in Figure 6. The display was restricted to the fundamental mode only from period of 5 to 200 s and suffices to reveal the impact of velocity changes brought out by the new models (Model 3, 4 and 5) to replace the correct one (Model 1). It is seen that scatter in the group velocities from one model to the other at any wave-period is very large and not as tolerable as obtained from the difference between Model 1 and 2 (see Fig. 3). For that none of the new test models (Model 3, 4 and 5) have the structural characteristic to substitute Model 1 in the inversion of source characteristics, we did not go further to test the performance of these models. The difference between Model 1 and 2 (see Fig. 1) reveals a good sense of least approximation that one should attain in the velocity structure. In the following, we further test the performance of Model 2 in replacing Model 1 in the inversion process.

FOCAL DEPTH DETERMINATION

We first need to give some succinct surface wave definitions. Cartesian components of a symmetric moment tensor due to a shear dislocation are described by the following equality (see Aki and Richards, 1980).

$$M_{ij} = M_o y_{ij}(\phi_s, \delta, \lambda) M(t), \quad i = 1,2,3 \quad j = 1,2,3 \qquad (1)$$

where M_o is moment, y_{ij} a functional of strike ϕ_s, dip δ, and rake λ and $M(t)$ the temporal variation of moment release. In Figure 2, the time derivative of $M(t)$ is displayed.

The surface wave complex spectral amplitudes in the three-component (u_L transverse, u_Z vertical and u_R radial component) are described, for example, in Aki and Richards (1980) and will not be repeated here. Using the complex spectral amplitudes the following system of linear equations can be written.

$$\begin{bmatrix} u_L(w_1) \\ u_Z(w_1) \\ u_R(w_1) \\ \vdots \\ u_L(w_n) \\ u_Z(w_n) \\ u_R(w_n) \end{bmatrix} = \boldsymbol{A} \begin{bmatrix} M_{11} \\ M_{12} \\ M_{13} \\ M_{22} \\ M_{23} \end{bmatrix} \qquad (2)$$

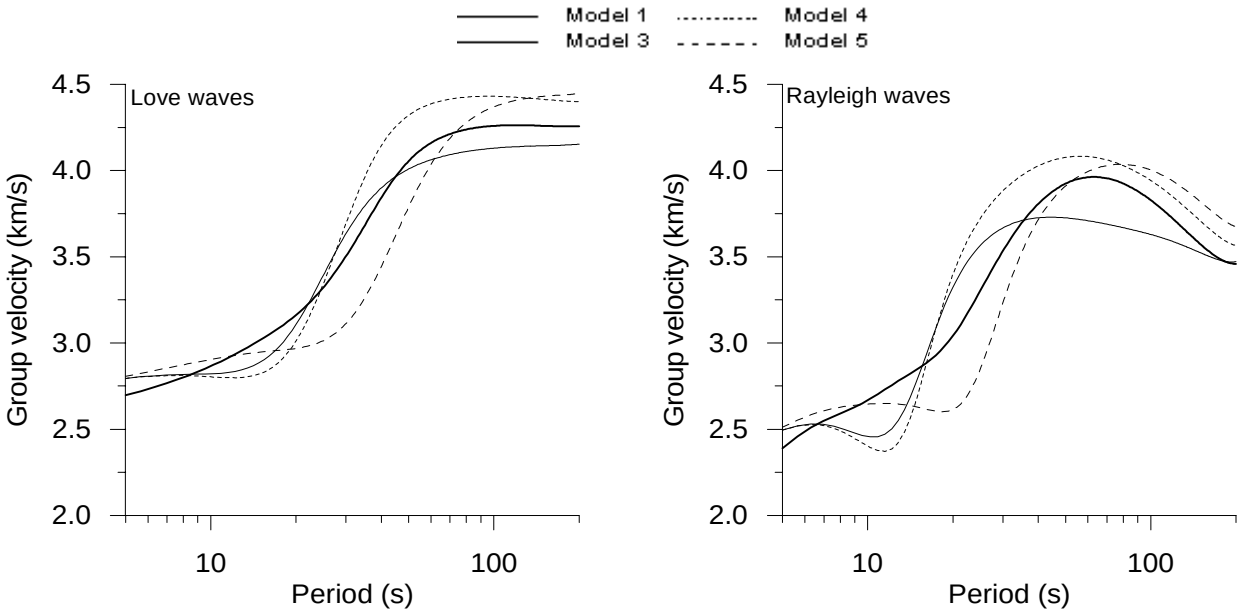

FIG. 6. Fundamental-mode Love and Rayleigh wave group velocities computed for the models shown in Fig. 5. See text for more explanation.

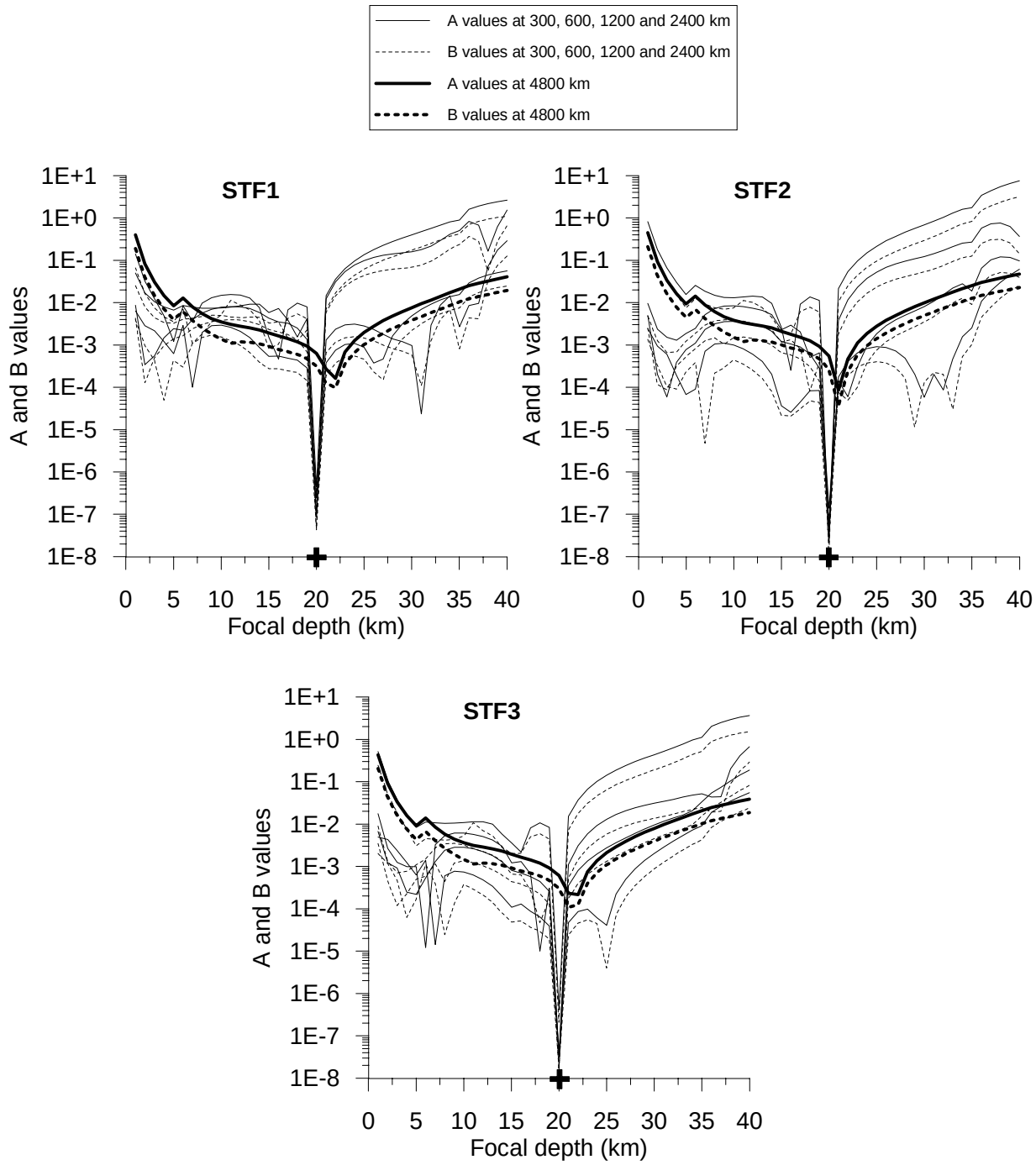

FIG. 7. Determination of focal depth from surface waves is illustrated. Focal depth is originally set to be 20 km and indicated sharply by the minima in the A and B values, but slightly incorrect one (22 km) at 4800 km distance is obtained.

where w is angular frequency taking n different values and the matrix $\boldsymbol{A}$ given in Jimenez *et al.* (1989). Rewriting in a closed form one has

$$\boldsymbol{U} = \boldsymbol{A}.\boldsymbol{M} \tag{3}$$

It is an over-determined linear system and can be solved by a linear least-square technique for $\boldsymbol{M}$ as follows (see Lay and Wallace, 1995).

$$\boldsymbol{M} = [\boldsymbol{A}^T \boldsymbol{A}]^{-1} \boldsymbol{A}^T \boldsymbol{U} \tag{4}$$

where the vector $\boldsymbol{U}$ contains the complex spectral amplitudes of an earthquake. In the theoretical tests, we obtain them from the synthetic seismograms.

The system in equation (3) is of complex form and can be separated into the real and the imaginary sub-systems. In order to obtain a correct focal depth from surface waves, Jimenez *et al.* (1989) has suggested an iterative method based on the separate inversions of the real and the imaginary parts of the system in equation (3). The idea is that, at the correct focal depth, each

sub-system converges to a common solution for the moment tensor elements (M_{ij}). At some trial focal depths, the following two parameters are computed and drawn against the focal depth.

$$A = \sum_{ij} \{(M_{ij}^R)^2 - (M_{ij}^I)^2\}, \quad B = \{(M_o^R)^2 - (M_o^I)^2\} \qquad (5)$$

where the symbols *R* and *I* denote the solutions obtained from the real and the imaginary sub-systems, respectively.

An illustration of the focal depth method is given in Figure 7. The focal depth was originally set to be 20 km, and the correct focal depth was searched in depths from 1 to 40 km in 1 km step. The *A* and *B* values obtained from the definitions in (5) are depicted by a different line pattern. Synthetic seismograms representing an earthquake recording at 70° station azimuth were computed utilizing the earth structure given by Model 1 in Figure 1. The focal depth search was performed for all the source time functions given in Figure 2. The A and B values corresponding to the synthetics at 300, 600, 1200 and 2400 km epicentral distances indicate sharply the correct focal depth at 20 km. However, those at 4800 km distance are not as sharp and indicate slightly incorrect focal depth at about 22 km, since the low period energy contribution at this distance somewhat decreases. Figure 7 shows that the focal depth method works quite accurately. But it should be mentioned that no erroneous assumption, as stated above, in place of the earth structure and the source time function was considered for the calculations given in Figure 7. In applications of the method to the real data, they may not be known exactly.

Now let us test the situation of which an incorrect source time function in equation (1) and an incorrect earth structure in equation (2) are taken instead of the correct ones. In Figure 8, we show the test results of focal depth, using STF2 as a correct one. Although the results for STF1 and STF3 are not shown here, they are very similar to the ones shown for STF2. In the inversion process, the correct earth structure given by Model 1 was replaced with the presumed approximation given by Model 2 (see Fig. 1). The correct source time function STF2 was replaced with the erroneous assumptions of a unit impulse located at the origin time, STF1 and STF3, respectively (see Fig. 2).

In Figure 8, we show the test results obtained at 600 and 4800 km epicentral distances. It is seen that the impulsive source totally fails to indicate the correct focal depth. On the other hand, STF1 and STF3 replacing STF2 come close to the indication of the correct focal depth at 20 km. The results at 600 km epicentral distance are better compared to the ones obtained at 4800 km. We did not show the focal depth tests for 300, 1200 and 2400 km epicentral distances, but they indicated focal depths in the range from about 15 to 25 km. Below the 300 km epicentral distance, the precision was greatly reduced, because of the limitation imposed on the period range. And also, the precision in the focal depth determination with the current approach decreased with the increase of the epicentral distance.

It should be noticed that the test results for STF1 and STF3 in Figure 8 are very similar. We have calculated spectra for each source time function in Figure 2 and seen that the corresponding spectral amplitudes exhibited considerable difference from each other at low periods. But also they replaced one another closely at large periods (e.g. greater than 20 s). This situation approximately is indicated by the dashed lines drawn across the amplitudes of STF1 and STF3 in Figure 2. It explains why those source time functions in Figure 2 replace one another in the inversion process. In addition, those secondary unit impulses located at 3 s in Figure 2, in contrast to the first ones located at the origin time, have equivalent spectral amplitudes to STF1, STF2 or STF3 at large periods as well. The focal depth tests using the second impulse at 3 s showed very similar results to the ones obtained with the source time functions in Figure 2. Since the first impulse located at the origin is dislocated in time, it does not represent the dominant amplitude distribution of the presumed source time functions.

The period range, that we have utilized for the calculations in Figure 8, runs from 20 to 100 s because of the reason explained in the normal mode section. The precision loss in the focal depth determination is primarily caused by this limitation due to the imposed structural error. The effect by the imposed error on the source time function stays secondary to the error in the velocity structure. A source time function matching the correct one in the rupture duration or a unit impulse correctly located in time generally suffices.

TEST INVERSIONS FOR RUPTURE MECHANISM

Once a focal depth is determined, a final inversion of the linear system in equation (3) with the combination of the real and the imaginary sub-systems is performed. The solution of this over-determined system for M_{ij} can be found with the application of equation (4). The principle axes (tension T, null axis N and pressure P) representing the best double-couple solution are found from an eigenvector decomposition of the inverted moment tensor M_{ij} (Jimenez *et al.*, 1989). The fault plane solution is determined by the interpretation of the principle axes in terms of strike, dip and rake. We will not make this interpretation, but present our synthetic inversion results in terms of the principle axes.

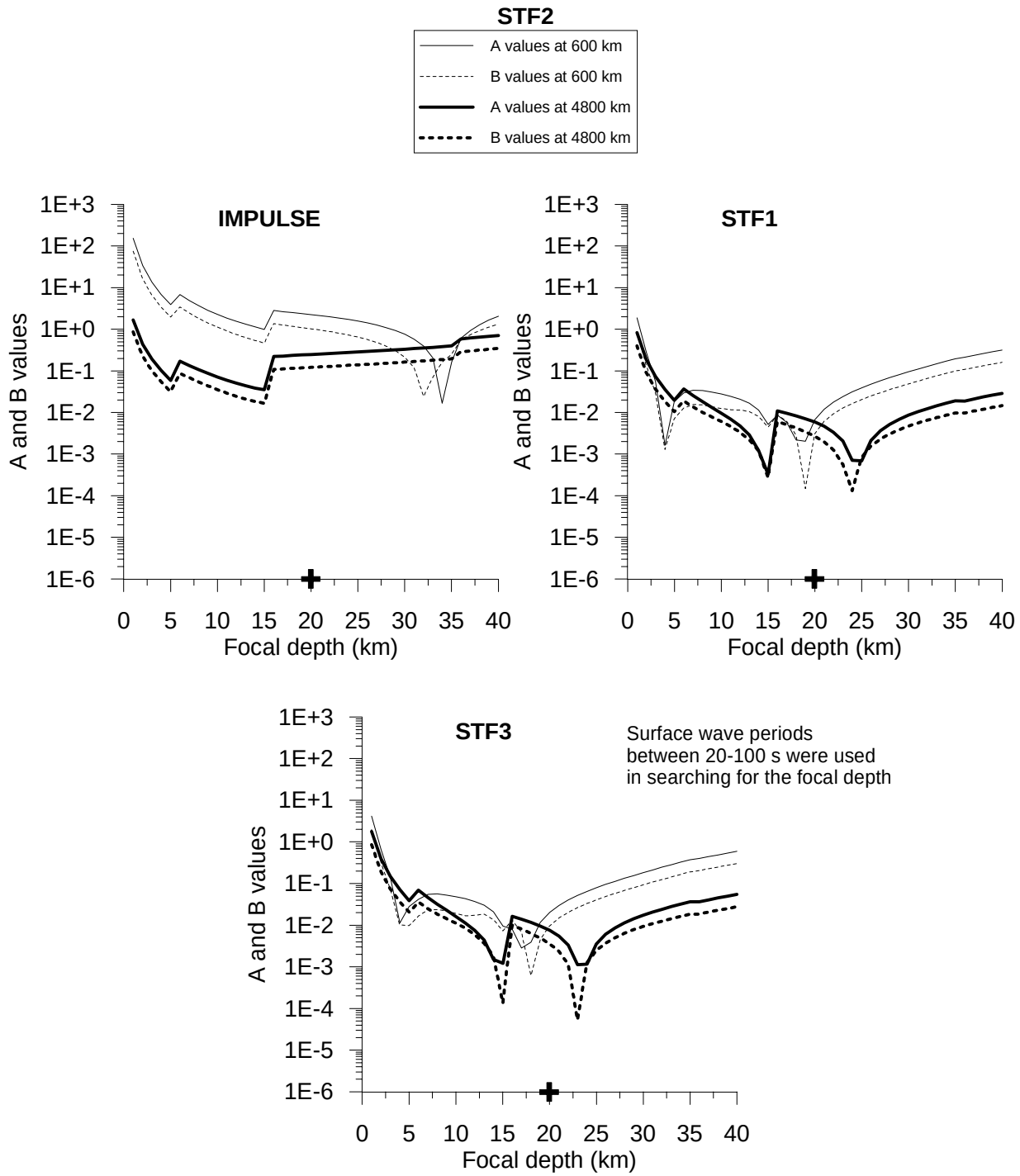

FIG. 8. Determination of focal depth from surface waves is illustrated. Model 2 replaces Model 1 (Fig. 1). A unit impulse located at the origin time, STF1 and STF3 (Fig. 2) respectively replace STF2. The approximations make the focal depth method less precise (compare with Fig. 5).

In order to demonstrate our inversion results in a statistical robustness we have selected three sample rapture mechanisms to test. The first one (MECH1) is a strike-slip fault, having strike = 180^o, dip = 90^o and rake = 180^o. The corresponding principle axes have the following azimuth and plunge in the lower-hemisphere of the focal sphere. Tension T: azimuth = 135^o and plunge = 0^o, null axis N: azimuth = 290^o and plunge = 90^o, Pressure P: azimuth = 45^o and plunge = 0^o. Note that any azimuth value for the null axis with plunge = 90^o would suffice and thus we have used an arbitrary one (e.g. 290^o). Notice also that, because of the geometry of the principal axes of MECH1, azimuth of tension axis around 315^o and azimuth of pressure axis around 225^o would also suffice after the inversion. Synthetic seismograms representing earthquake recordings at a

focal depth of 20 km were calculated at 70° station azimuth by employing Model 1 in Figure 1 to represent the earth structure.

We have summarized the inversion results for the first rupture mechanism in Table 1. The inversion was performed for all the selected epicentral distances and the source time functions. We have seen in the previous section that the focal depth determination has some bias due to the period limitation. For that reason, we have performed the inversion at focal depths of 15, 20 and 25 km, in order to see the impact of using a slightly incorrect focal depth. In the inversion, Model 1 was replaced with the erroneous Model 2 (Fig. 1). We have used the correct and the incorrect source time functions and seen that there was no significant difference in using a correct or an incorrect one. Therefore, in Table 1, we have not made a classification with respect to the source time function and the listed numbers reflect averages. The erroneous assumption made by an impulsive source located at the origin time in place of STF1, STF2 or STF3 (Fig. 2) resulted in a rupture mechanism very close to a dip-slip (against the original strike-slip) striking differently.

It is seen in Table 1 that all the inversion results are reasonable, but there are some differences in the precision with respect to the epicentral distance and the focal depth. In general, the results are more accurate with the increase of focal depth. Although the focal depth was originally set to be 20 km, the results at 25 km focal depth are more accurate. In addition, similar to the case seen above in the focal depth method, the inverted rupture mechanisms lose precision with the increase of epicentral distance, except at 300 km distance. Considering the very low period range utilized in the inversion for 300 km distance the obtained results in Table 1 are indeed surprising. This shows that a low period range such as from about 20 to 25 s is sufficient for an approximate inversion of the rupture mechanism.

The second rupture mechanism (MECH2) tested in the inversion is an oblique-reverse fault, having strike = 270°, dip = 45° and rake = 65°. The corresponding principle axes have the following azimuth and plunge values. Tension T: azimuth = 99° and plunge = 72°, null axis N: azimuth = 288° and plunge = 17°, Pressure P: azimuth = 198° and plunge = 3°. Synthetic seismograms representing earthquake recordings at a focal depth of 20 km were calculated at a station azimuth of 135° by utilizing Model 1 in Figure 1 and STF2 in Figure 2. Model 2 in Figure 1 and STF1 in Figure 2 were assumed to erroneously replace the true ones in the inversion process. Since it was experienced in MECH1 that using different source time functions were not much effective on the inversion results, we have limited the erroneous assumption made for the source time function to STF1 only, which helped save considerable computational time.

Table 2 summarizes the inversion results for the second rupture mechanism. Since, in this mechanism as well, the focal depth method has resulted in focal depths around 5 ± 20 km, we have again performed the inversion at three different focal depths as listed in Table 2. Similar to the first rupture mechanism we have obtained reasonable inversion results in the second one as well. In contrast to the first mechanism, the inversion performed at focal depth of 25 km yielded relatively poor results and those obtained at the correct focal depth (20 km) resulted in relatively better resolution. On the other hand, it is seen from Table 2 that the differences in the inverted rupture mechanisms throughout focal depths tested are not very large. Overall performance of the method under the presumed conditions is reasonably well.

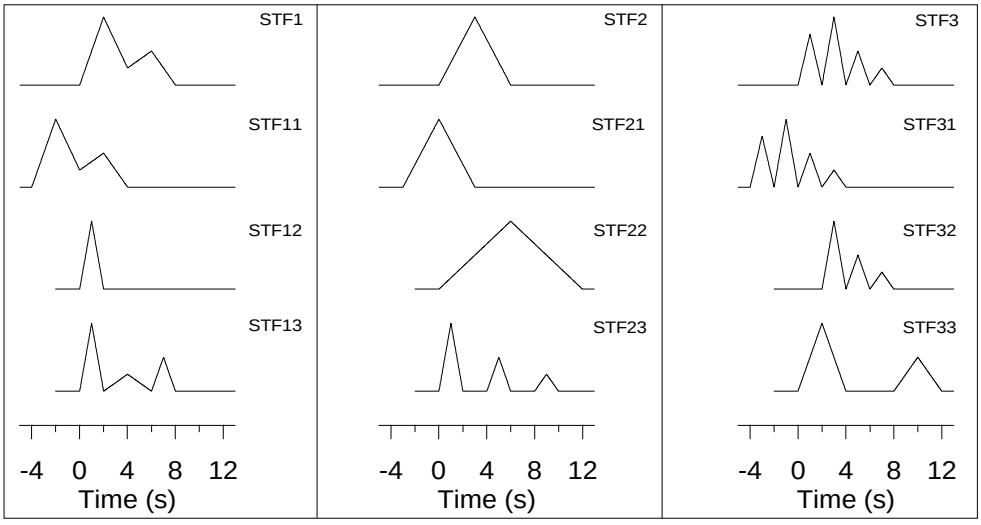

FIG. 9. Various source time functions tested in the inversion of source characteristics. See text for more explanation.

Table 1. List of inverted principles axes for MECH1. Azimuth (Azm) and plunge (Plg) of the principle axes (Tension T, null axis N and Pressure P) in the lower-hemisphere of the focal sphere are shown. The true values are T: Azm = 135^o and Plg = 0^o, N: Azm = 290^o and Plg = 90^o, P: Azm = 45^o and Plg = 0^o.

Focal Depths		Epicentral distance									
		R=300 km		R=600 km		R=1200 km		R=2400 km		R=4800 km	
		Azm	Plg	Azm	Plg	Azm	Plg	Azm	Plg	Azm	Plg
H=15 km	T	308	15	127	5	128	10	127	15	124	16
	N	120	76	299	86	302	80	297	75	285	74
	P	218	2	37	1	38	1	36	2	33	5
H=20 km	T	134	12	134	3	134	5	133	10	130	15
	N	290	78	288	87	296	85	270	79	276	73
	P	43	5	44	1	44	2	42	4	37	10
H=25 km	T	139	4	138	2	139	3	137	6	132	10
	N	282	86	278	88	288	87	281	83	269	77
	P	48	3	48	1	49	2	47	4	41	9

Table 2. List of inverted principles axes for MECH2. The true values are T: Azm = 99^o and Plg = 72^o, N: Azm = 288^o and Plg = 17^o, P: Azm = 198^o and Plg = 3^o. The same notations in Table 1 are used.

Focal Depths		Epicentral distance									
		R=300 km		R=600 km		R=1200 km		R=2400 km		R=4800 km	
		Azm	Plg	Azm	Plg	Azm	Plg	Azm	Plg	Azm	Plg
H=15 km	T	96	81	95	79	95	78	91	78	84	78
	N	293	9	294	11	293	11	294	11	295	10
	P	202	3	203	4	203	4	204	5	204	6
H=20 km	T	88	77	87	75	87	75	84	74	77	74
	N	292	12	295	13	294	14	296	14	297	12
	P	201	5	203	7	203	7	204	8	205	10
H=25 km	T	75	67	77	66	76	65	75	65	71	65
	N	259	23	271	23	268	25	273	24	278	23
	P	169	2	179	5	176	5	179	7	184	10

Table 3. List of inverted principles axes for MECH3. The true values are T: Azm = 340^o and Plg = 35^o, N: Azm = 222^o and Plg = 34^o, P: Azm = 102^o and Plg = 37^o. The same notations in Table 1 are used.

Focal Depths		Epicentral distance									
		R=300 km		R=600 km		R=1200 km		R=2400 km		R=4800 km	
		Azm	Plg	Azm	Plg	Azm	Plg	Azm	Plg	Azm	Plg
H=15 km	T	331	52	336	49	336	49	336	51	332	56
	N	209	23	312	26	212	26	212	24	212	19
	P	105	29	106	29	106	29	108	29	112	27
H=20 km	T	337	41	340	39	340	39	340	41	340	45
	N	222	27	224	28	224	28	223	28	222	25
	P	109	38	109	38	109	38	110	37	114	35
H=25 km	T	343	32	345	31	346	31	346	32	347	35
	N	228	35	230	35	230	35	230	36	228	35
	P	104	39	105	40	105	39	105	38	108	36

Table 4. Effect of various source time functions (first column in Fig. 9) on MECH1 is shown. Refer to Table 1 for explanation.

Source Time Functions		Epicentral distance									
		R=300 km		R=600 km		R=1200 km		R=2400 km		R=4800 km	
		Azm	Plg	Azm	Plg	Azm	Plg	Azm	Plg	Azm	Plg
STF11	T	331	28	326	45	330	46	327	42	324	42
	N	76	25	88	29	76	15	74	18	71	18
	P	200	51	198	32	179	40	181	43	179	43
STF12	T	326	21	317	41	320	57	317	55	314	63
	N	95	59	108	45	94	24	94	27	88	20
	P	227	22	214	15	193	21	195	21	185	18
STF13	T	315	8	317	3	307	4	126	5	132	0
	N	113	82	109	87	116	86	299	85	229	86
	P	225	3	227	2	217	1	36	1	42	4

Table 5. Effect of various source time functions (second column in Fig. 9) on MECH2 is shown. Refer to Table 2 for explanation.

Source Time Functions		Epicentral distance									
		R=300 km		R=600 km		R=1200 km		R=2400 km		R=4800 km	
		Azm	Plg	Azm	Plg	Azm	Plg	Azm	Plg	Azm	Plg
STF21	T	228	43	210	58	171	59	222	55	131	53
	N	102	32	100	12	275	8	105	18	269	29
	P	350	30	3	30	10	30	5	29	11	21
STF22	T	51	53	51	55	30	76	32	76	45	59
	N	277	28	289	20	123	1	301	0	293	13
	P	174	23	188	27	213	14	211	14	197	28
STF23	T	67	37	81	65	97	75	96	75	77	67
	N	239	52	262	25	291	15	297	14	274	22
	P	334	4	172	0	200	4	206	5	182	6

Table 6. Effect of various source time functions (third column in Fig. 9) on MECH3 is shown. Refer to Table 3 for explanation.

Source Time Functions		Epicentral distance									
		R=300 km		R=600 km		R=1200 km		R=2400 km		R=4800 km	
		Azm	Plg	Azm	Plg	Azm	Plg	Azm	Plg	Azm	Plg
STF31	T	332	20	335	23	333	29	336	24	335	24
	N	237	14	243	5	63	0	243	7	238	13
	P	115	66	141	66	153	61	137	65	122	62
STF32	T	310	64	310	69	349	15	266	65	285	73
	N	213	4	204	6	234	58	44	19	25	3
	P	121	26	111	21	89	28	139	16	116	17
STF33	T	298	63	300	65	345	41	273	64	291	71
	N	34	3	207	1	221	33	34	14	27	2
	P	126	27	116	25	108	32	130	21	118	18

We have tested a third rupture mechanism (MECH3) and the inversion results for this one are listed in Table 3. The model parameters employed in the synthetic and the inversion calculations were kept similar to the ones considered in the first two mechanisms above. The station azimuth in this test was set to be 250^o. The current mechanism represents a vertical-slip fault with some oblique component and has strike = 135^o, dip = 30^o and rake = 0^o. The corresponding principle axes have the following azimuth and plunge values. Tension T: azimuth = 340^o and plunge = 35^o, null axis N: azimuth = 222^o and plunge = 34^o, Pressure P: azimuth = 102^o and plunge = 37^o. In this test as well, the inverted rupture mechanisms show reasonable resolution of the principle axes of the original mechanism. The results obtained at focal depth of 25 km, in contrast to the ones obtained at the correct focal depth (20 km), indicate relatively better resolution.

The inversion results (Table 1, 2 and 3) illustrated in a statistical manner demonstrate that the single-station inversion of surface waves for the rupture mechanism produces reasonably efficient solutions under reasonable approximations made for the earth structure and the source time function. The second impulse located at 3 s in Figure 2 works efficiently in the inversion of rupture mechanism, but a few seconds shift to the right or left (e.g. ± 2 s) causes significant precision loss. It should be noted that the station azimuth is not a primary concern in a single-station approach. Any value of the station azimuth other than ones used above yields very similar inversion results to the ones listed in Table 1, 2 and 3. On the other hand, Rayleigh or Love surface waves of an earthquake observed at a station azimuth near to one of the nodal planes of the rupture mechanism are likely to be reduced in signal-to-noise ratio. Intrinsically this may cause precision loss in the inversion.

Additional test source time functions

In the previous discussions of this section, we have examined source time functions that replaced one another efficiently in the period range (i.e. 20-100 s) utilized in the inversion. We now move to more source time functions that may not replace one another in the inversion. In Figure 9, we display 9 additional source time functions along with the ones considered earlier (Fig. 2). The figure is so designed that the new functions in each column subsequently will be employed to replace the early ones shown on the top row. For example, STF11, STF12 and STF13 will be used in place of STF1 in the inversion of rupture mechanism.

Note that the replacement source time functions given in the second row of Figure 9 (STF11, STF21 and STF31) represent time shifts to the left equivalent to half the rupture duration. This situation may correspond to an error made in the determination of origin time by a few seconds. In the third row of Figure 9, the source time functions are either short (STF12) or long (STF22) compared to the original one in rupture duration. In the case of STF32, the first pulse is missing from the original function. The remaining source time functions (STF13, STF23 and STF33) given in the fourth row of Figure 9 were arranged arbitrarily with no specific characteristic relevant to the original one.

Table 4 summarizes the inversion results related to STF1. In the current calculations, the rupture mechanism was assumed to be MECH1 as described above and the other modelling parameters were taken similar to the ones utilized in Table 1. In the current and the following two tables, we are primarily interested in the precision of the inverted rupture mechanisms after the above-mentioned replacements for the source time functions. In order to prevent the tables from numbers clutter we did not employ a classification with respect to the focal depth, but the source time function only. In each case, a separate focal depth test was performed and the corresponding focal depth was determined from the minima in the A and B value curves (e.g. see Figs. 7 and 8). In the synthetic seismograms, we again set the focal depth to be 20 km. Majority of the focal depth tests have indicated a focal depth around 10 ± 20 km, but in a few cases it was indicated as shallow as 5 km or as deep as 55 km.

It is seen in Table 4 that STF11 and STF12 do not replace STF1 in the inversion. The inverted principle axes are significantly different from the ones originally considered in the focal area. An error in the origin time by a few seconds (STF11) or a relative mismatch in the rupture duration (STF12) caused significant failure in the method. On the other hand, notice that STF13, which was produced from STF12 by the addition of two pulses (Fig. 9), efficiently replaced STF1, which is seen from the comparison of the inverted principle axes.

In Table 5, we summarize the inversion results obtained for STF2. The rupture mechanism in the focal area was represented by MECH2 described above. In this table as well, the case of an error in the origin time (STF21) or a mismatch in the rupture duration (STF22) resulted in significant failure. It is noted that the rupture duration in STF22 is longer than the one in STF2, which is opposite to the case between STF1 and STF12 (Fig. 9). The third replacement in this group is STF23, which was formed by a three-pulse sequence against the

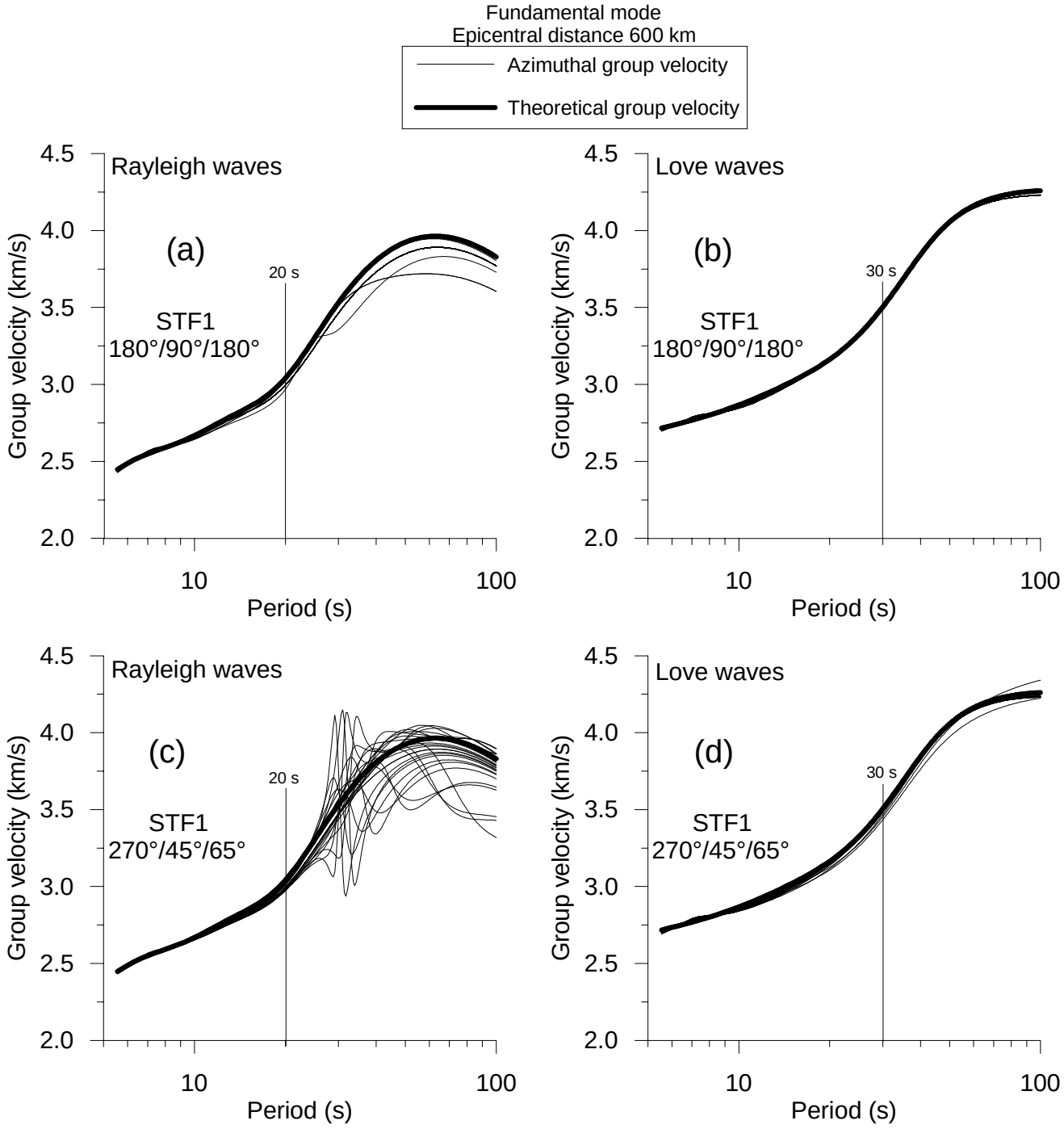

FIG. 10. Effect of the source phase shift on the observed group velocities calculated at 600 km epicentral distance is shown. The cases in (a) and (b) are degenerate, and (c) and (d) non-degenerate. See text for more explanation.

Table 7. Source parameters of events used in the inversion of source characteristics.

	Date	Origin Time (UTC)	Latitude (N^o)	Longitude (E^o)	Azimuth (^{o})	Distance (km)	Depth (km)	M_S	Location
1	10/13/1997	13:39:36.03	36.35	22.11	66	1619	13	6.5	Greece
2	03/14/1998	19:40:27.05	30.15	57.61	312	2008	9	6.9	Iran

Parameters were taken from IRIS (Incorporated Research Institutions for Seismology).

original one (STF2) formed by a relatively broad single-pulse. Because both the total rupture duration and the amplitude envelope do not match, the inverted principle axes show some inconvenience at particularly 300 km epicentral distance. Resolution at the other distances does not indicate a significant failure, but is not as efficient as desired.

In Table 6, the inversion results for STF3 are shown. The rupture mechanism was assumed to be MECH3 as described above. It is observed that the constant time shift in STF31 relative to STF3 similarly produces unacceptable inversion results. The case of a missing pulse considered with STF32 is also a failure. As a matter of fact, STF32 behaves more like a constant time shift (i.e. 2 s) than simply a missing pulse. The last case in this sequence is STF33, which is formed by a combination of two individual broad pulses separated largely in time. The inverted principle axes at 1200 km epicentral distance are surprisingly well resolved, but the remaining ones at the other distances are not as well as desired.

DISCUSSION OF SINGLE-STATION GROUP VELOCITY INVERSION

The model structure representing the real earth should be chosen using any seismological data available in the region of interest. The inversion technique analysed in this work will yield more accurate results if the crustal thickness and the average velocities in the crust and the upper-mantle reasonably are chosen. In a final step, *a posterior* match between synthetic seismograms, computed after the inversion, and actual recordings can be used to check the validity of the made assumptions *a priori* (Dufumier *et al.*, 1997).

Another approach could be the single-station inversion of the observed surface wave group velocities to estimate the shear velocities of the propagation media, such as applied in the current study. This approach suffers from the well-known phase shift that earthquake waves acquire at the focal area with period dependence (Dziewonski and Hales, 1972; Çakir *et al.*, 2000b). In the following, we highlight problems of this procedure. Earthquake rapture mechanisms can be divided into two groups, with respect to phase spectrum that they yield at the source with wave-period dependence. The rupture mechanisms of strike-slip and normal or thrust faults dipping 45^o are called degenerate and the respective source phase spectrum after these mechanisms does not change with period (see Levshin *et al.*, 1999). The second group, which is called non-degenerate, includes all the other rupture mechanisms having various fault plane orientations. In this group, the source phase changes significantly with period.

In order to better explain the above-discussed situations, we have performed some numerical calculations as shown in Figures 9a-d. Using the definitions related to the source phase spectra by Levshin *et al.* (1999) we have computed the theoretical group velocities after affected by the source phase shift at different azimuths of the fault plane. In the calculations, Model 1 shown in Figure1 was used to represent the earth structure, and the epicentral distance was set to be 600 km. Figures 9a and 9b represent the non-degenerate case ($180^o/90^o/180^o$) and Figures 9c and 9d the degenerate one ($270^o/45^o/65^o$) where numbers in the parentheses denote strike, dip and rake. The station azimuth was varied from 0^o to 345^o in 15^o step. The group velocity curves depicted by a solid line are the theoretical ones belonging to Model 1 with no phase effect from the source. Those thin-lined curves described as Azimuthal group velocity represent the effect of the source phase shift on the observed group velocities.

It is noted that Rayleigh surface waves are affected by the source phase shift more (Figs. 9a and 9c) than Love waves (Figs. 9b and 9d). In addition, the degenerate case is affected by the source phase shift less (Figs. 9a and 9b) than the non-degenerate one (Figs. 9c and 9d). The Azimuthal phase effect becomes severe for Rayleigh waves above period of about 20 s (Fig. 9c). This situation occurs in Love waves above about 30 s, but not as prominent as in Rayleigh waves. In the calculations of Figs. 9a-d, the focal depth was set to be 20 km. Some other shallower focal depths such as 5, 10 and 15 km were also tested in this respect. It was seen that the Azimuthal group velocities at gradually lower wave-periods were also affected by the source phase shift since then the focal depth was shallow enough to trigger low-period surface waves (e.g. less than 20 s) as well.

We have tested several other choices of the degenerate and the non-degenerate cases in place of the ones given in Figures 9a-d and seen that similar features shown in Figures 9a-d were also present. It was also seen that a small deviation from a non-degenerate fracture mechanism causes significant source phase effect on the Azimuthal group velocities of particularly Rayleigh waves. In addition, it should be noted that the effect of the source phase shift is proportional to the epicentral distance and decreases appreciably with increasing epicentral distance. From the highlights of the current calculations it is reasonable to suggest that the single-station inversion of particularly Love wave fundamental mode can be used

to predict the seismic velocities of the propagation media. Prediction error decreases with decreasing wave-period and also with increasing epicentral distance. Azimuthal group velocities of Rayleigh surface waves below about period of 100 s, even in the non-degenerate case, are usable in predicting the velocity structure beyond about 5000 km epicentral distance because the effect of the source phase shift significantly decreases at far distances. In this study, we utilize Love wave fundamental mode only in predicting the velocity structure because of relatively small epicentral distances of the selected events.

APPLICATION TO ACTUAL RECORDS

We have selected two regional earthquakes to test the performance of the current method. Table 4 lists event parameters. Three-component surface wave recordings of these events at the station TBZ (39.77^{o}N, 40.99^{o}E) are utilized in the inversion. Using the station azimuth the horizontal components are first vector-rotated to theoretical transverse and radial components. Rayleigh waves in the vertical-component and Love waves in the transverse-component are employed in the inversion. Considering the presumed effect of 3-D heterogeneity in the earth structure we have not included the radial-component in the calculations, which causes no loss of generality.

The earthquake recordings are digital broadband with a Nyquist frequency of 25 Hz. Güralp CMG-40s seismometers with a flat velocity response between 0.05 and 20 Hz were used. Instrumentally corrected seismograms are first time-windowed with apparent group velocity between selected maximum (5 km/s) and minimum (2 km/s) velocities and then decimated down to a sampling rate of 1 s along with the application of a low-pass filter at 0.425 Hz cut-off frequency. A computer program package called Computer Programs in Seismology by Hermann (1987) is employed for the multiple filter technique. The observed Rayleigh and Love wave group velocity curves are obtained from the contour diagrams produced by this program package.

We will follow a chronological order in evaluating the actual records. The first step is to estimate the velocity-depth distribution along the propagation path, directly from the inversion of the observed group velocities. In this stage, we will perform three separate group velocity inversions, i.e. using Rayleigh waves alone, Love waves alone and Rayleigh and Love waves together. In the group velocity inversion, the least-square technique described by Tarantola (1987) and the corresponding partial derivatives with respect to underground shear velocities derived by Takeuchi and Saito (1972) will be employed. In the second step, the estimated velocity structure will be utilized to predict the focal depth. Finally, taking the necessary measures discussed in the sections above we will solve the rupture mechanism. In order to approximately eliminate the propagation effect of absorption (e.g. see Jimenez *et al.,* 1989) we will employ the shear wave quality factors reported by Mindevalli (1988) for the lithosphere structure beneath the Anatolian plate. Apparent quality factors of surface waves are computed by utilizing the variational principle as described in Aki and Richards (1980).

In preparing the surface wave records for the multiple filtering, we did not correct for the effect of the source phase shift. In terms of the source time function alone, this corresponds to indirectly assuming a unit-step dislocation pulse at the source. For example, let us assume that, as generally occurs, the source time history actually has a certain rise-time (e.g. 6 s) other than the assumed unit-step. In this configuration, the half duration of the actual pulse is 3 s and the assumed one 0 s, which is of a 3-s difference that cannot be ignored in the inversion of the rupture mechanism as highlighted above in the source time section. In addition, it should be noted in the following calculations that the observed group velocities of the fundamental mode are very weakly sensitive to sharp velocity contrasts and mostly sensitive to the averages of the profile over broad depth ranges because they are functionals of the velocity profiles involving integrals over the velocity-depth profile (e.g. see Çakir *et al.,* 2000a). The inversion results of the observed group velocities should be judged from this point of view, e.g. depth to the Moho discontinuity and the velocity contrasts may not be satisfactorily resolved.

Greece-13 October 1997 earthquake

The current event is due to the seismic activity of the African plate subducting underneath the Aegean plate along the Hellenic arc, which gives rise to thrust faulting in the trench region and normal faulting in back arc regions (e.g. Papazachos *et al.,* 1991; Yilmaztürk *et al.,* 1999). The wave path of this event to the station TBZ corresponds to the relatively tectonically homogeneous lithosphere structure beneath that of the southern Aegean Sea and the Anatolian plate (e.g. see Yilmaztürk *et al.,* 1999).

In Figure 11, we depict the observed group velocity inversion results. It is seen in Figure 11a that the three estimated velocity structures are somewhat different from each other. This is mainly caused by the source phase shift that effects Rayleigh and Love waves in a different level as already discussed in the previous

section. We have shown that Love waves were least affected by the source phase shift as compared to Rayleigh waves. This means that the velocity structure obtained after the inversion of the observed Love wave group velocities represents the most correct estimation of the medium (Fig. 11a). Figure 11b shows the observed and the theoretical dispersion curves in which the theoretical one is calculated by using the velocity-depth profile in Figure 11a corresponding to the Love-wave inversion alone. It is noted that the observed Rayleigh wave dispersion curve poorly follows the theoretical one, which clearly indicates the different level of the source phase effect on Rayleigh waves.

We now move to the determination of focal depth and rupture mechanism and employ the Love-wave velocity structure shown by the thin-straight line in Figure 11a. Considering the possibility of which the inverted velocity-depth distribution consists some error, we will perform the inversion of source characteristics using some different minimum wave-periods, i.e. 20, 25, 30 and 35 s. We next face the problem of selecting a source time function, which should properly replace

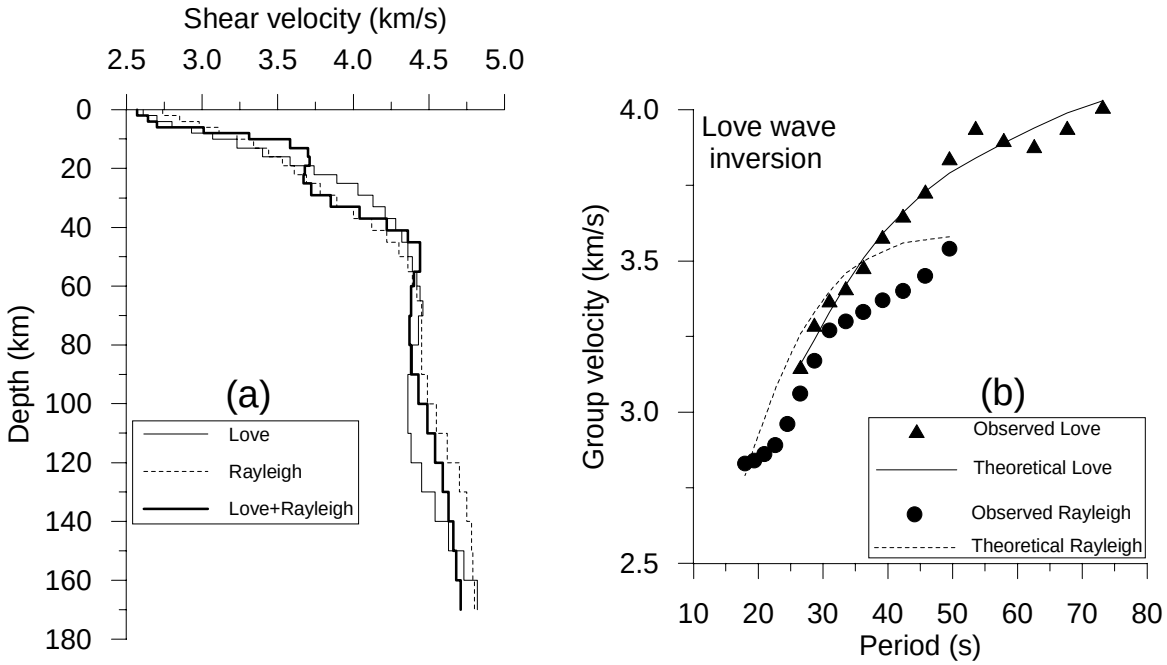

FIG. 11. Results of shear velocity inversion using the observed group velocities of the first event listed in Table 7 are shown. a) Inverted velocity-depth profiles and b) The observed and the theoretical group velocity curves. See text for more explanation.

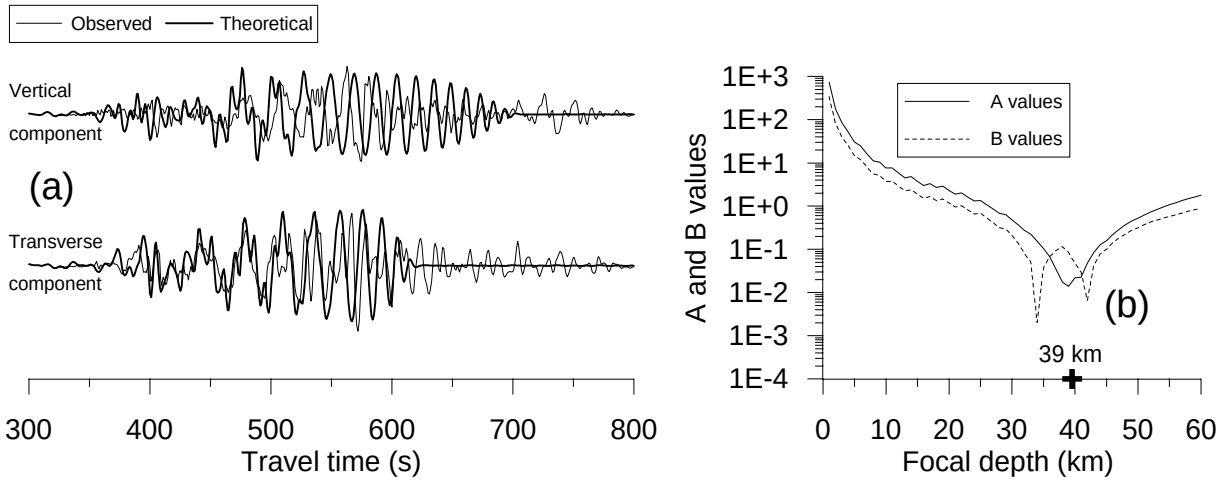

FIG. 12. a) Result of synthetic seismogram modeling for the first event in Table 7 and b) The corresponding A and B value curves showing the focal depth at 39 km.

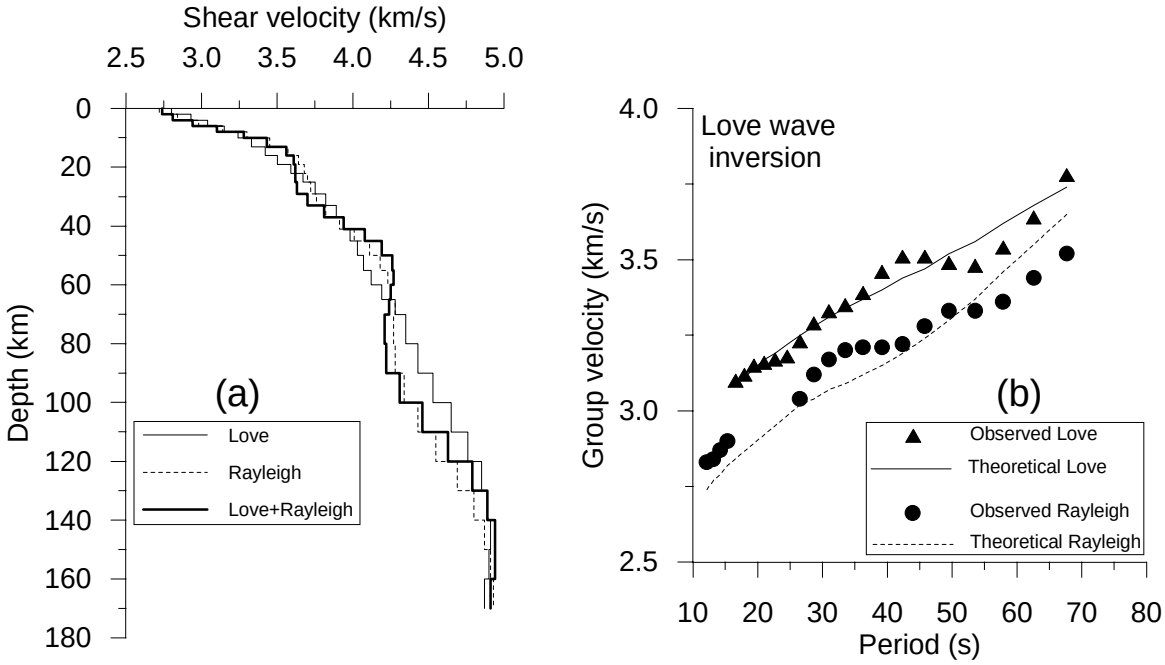

FIG. 13. Results of shear velocity inversion using the observed group velocities of the second event listed in Table 7 are shown. a) Inverted velocity-depth profiles and b) The observed and the theoretical group velocity curves. See text for more explanation.

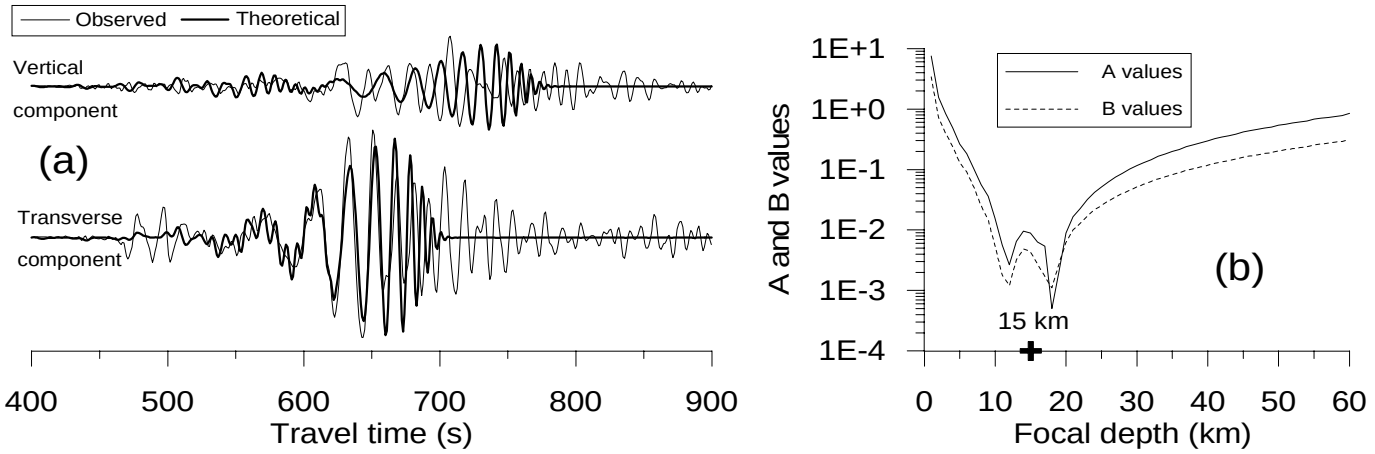

FIG. 14. a) Result of synthetic seismogram modeling for the second event in Table 7 and b) The corresponding A and B value curves showing the focal depth at 15 km.

the true one. One should note that whatever a source time function is chosen, it should accommodate the necessary time shift to the left on time axis, in order to alleviate the impact of the unit-step function initially presumed in obtaining the observed group velocities. For example, if the actual source time function is a triangular pulse of duration 6 s centering at 3 s, then the one replacing it in the inversion should have about the same duration but center around 0 s.

Upon some sequence of trial-and-error inversions and synthetic seismogram calculations we have decided that a simple triangular pulse of duration around 6 s centered at the origin time (0 s) suffices for the current event. The pulse duration was decided when matching particularly higher mode amplitudes. In Figure 12a, we illustrate the result of five-mode synthetic seismogram modeling and in Figure 12b the result of the focal depth search, which indicates a value around 39 km. The inverted fault plane parameters are listed in Table 8. In the table, three other fault plane solutions as reported by the indicated seismological sources are also given. We will not deal with the details of the procedure applied by those institutions in obtaining their solutions, but use them for the purpose of comparison only.

It is seen from Table 8 that the fault plane solution (i.e. NP2) represents a low-angle thrust fault, which corresponds to the trench area of the Hellenic arc (e.g. see Yilmaztürk *et al.,* 1999). All the solutions have comparable dip and rake values, but the strike directions vary to some degree. Some different focal depths located in the lower crust are reported for this event: Harvard CMT (44 km), ISC (26 km), GFZ Postdam (31 km) and the current study (39 km).

It is seen from Figure 12a that the synthetic seismogram modeling show some inconvenience at particularly low wave-periods. The velocity structure above depth of about 20 km are not well resolved in the Love-wave group velocity inversion because the low wave-periods, which would better resolve the velocities at this depth range, could not be recovered efficiently after the multiple filtering. This could be caused by the wave propagation across the different crustal structures beneath that of the Aegean basin and the Anatolian peninsula. Note that the observed Love-wave group velocities used in the inversion have wave-periods as low as 25 s only (see Fig. 11b). In the inversion of source characteristics, we have taken the minimum wave-period as 35 s greater than the one suggested by the synthetic modeling above (20 s), since otherwise the stability of the method was greatly reduced in the determination of both rupture mechanism and focal depth. On the other hand, excluding the small wave-periods from the inversion caused significant precision loss in particularly the strike direction, which can be seen from comparing the current solutions to the other ones in Table 8.

Table 8. Fault plane solutions of the first event listed in Table 7.

	Strike	Dip	Rake	
Current Study	72	66	90	NP1
	255	24	92	NP2
Harvard CMT	119	70	90	NP1
	296	20	90	NP2
ISC	115	71	101	NP1
	264	22	61	NP2
GFZ Postdam	150	70	105	NP1
	292	25	55	NP2

We have performed some other test calculations utilizing the other two models shown in Figure 11a. The focal depth method was affected the most by the new models and indicated a value around 43 km, but some other spurious minimums rather than an isolated one such as obtained in Figure 12b in the A and B value curves were also present which made it difficult to figure out the focal depth. On the other hand, the inverted fault planes were not so different from the ones obtained above using the Love-wave structure (Table 8). The Rayleigh-wave velocity structure (dashed-line in Fig. 11a) resulted in some additional oblique component in the rupture mechanism.

Iran-14 March 1998 earthquake

The motion of the Arabian plate towards about northeast builds significant thrust along the Bitlis and Zagros belt. The plate movements farther in the northeast corresponding to the regions of the Greater and the Lesser Caucasus, the Kopet Dagh and the Elburz Mountains are of complex form yielding thrust belts towards concurrently north and south. As a result, part of southern Iran, bounded by the active tectonics of the Bitlis and Zagros and the Kopet Dagh thrust belts, undergoes compressive regime (e.g. see Yilmaztürk *et al.,* 1999). This compression causes some regional intra-plate strike-slip faults that extend from approximately north to south. The current event is due to the seismic activity occurred in this region. The wave path of this event to the station TBZ corresponds to the relatively tectonically hetero-geneous lithosphere structure beneath that of the western Iran and the eastern Anatolia.

In Figure 13, we depict the observed group velocity inversion results. It is again seen in Figure 13a that the three estimated velocity structures are different from each other. The source phase shift effects Rayleigh and Love waves in a different level. The velocity structure obtained after the inversion of the observed Love wave group velocities represents the most correct estimation of the medium (Fig. 13a). Figure 13b shows the observed and the theoretical dispersion curves in which the theoretical one is calculated by using the velocity-depth profile in Figure 13a corresponding to the Love-wave inversion alone. It is again noted that the observed Rayleigh wave dispersion curve relatively poorly follows the theoretical one.

For the determination of focal depth and rupture mechanism we will employ the Love-wave velocity structure shown by the thin-straight line in Figure 13a and perform the source inversion using the similar minimum wave-periods, i.e. 20, 25, 30 and 35 s. Upon some sequence of trial-and-error inversions and synthetic seismogram calculations we have decided that a simple triangular pulse of duration around 8 s centered at the origin suffices for the current event. The pulse duration was decided when matching particularly higher mode amplitudes. In Figure 14a, we illustrate the result of five-mode synthetic seismogram modeling and in Figure 14b the result of the focal depth search, which

indicates a value around 15 km. The inverted and the other three fault plane solutions as reported by the indicated institutions are listed in Table 9.

It is seen from Table 9 that the fault plane solutions except the ones reported by GFZ Postdam closely represent strike-slip faulting which corresponds to the compressive tectonics in southern Iran. CMT, ISC and the current solution have comparable strike, dip and rake values. Note that NP2 in the current solution strikes in the opposite direction to the ones reported by Harvard CMT and ISC, which explains the sign difference in the rake values (see Table 9). The GFZ Postdam solution (i.e. NP1) is more like a vertical-slip fault with a small accompanying strike-slip component. Some similar focal depths in the upper crust are reported for this event: Harvard CMT (15 km), ISC (9 km), GFZ Postdam (15 km) and the current study (15 km).

Table 9. Fault plane solutions of the second event listed in Table 7.

	Strike	Dip	Rake	
Current	157	84	160	NP1
Study	252	70	6	NP2
Harvard	154	57	-174	NP1
CMT	61	85	-33	NP2
ISC	146	58	-179	NP1
	56	89	-32	NP2
GFZ	287	87	-113	NP1
Postdam	191	23	-7	NP2

It is seen from Figure 14a that the synthetic seismogram modeling show some inconvenience for particularly low period Rayleigh waves. The velocity structure above depth of about 15 km are not well resolved in the Love-wave group velocity inversion because the low wave-periods, which would better resolve the velocities at this depth range, could not be recovered efficiently after the multiple filtering. This is probably caused by the irregular geology in the upper crust as a result of the active tectonics in the region. Note that the observed Love-wave group velocities used in the inversion have wave-periods as low as 15 s only (see Fig. 13b). In the inversion of source characteristics, we have taken the minimum wave-period as 20 s as suggested by the synthetic modeling above and the stability of the method was greatly reduced when wave-periods below 20 s were included in the inversion.

We have performed some other test calculations utilizing the other two models shown in Figure 13a. The focal depth method was again affected the most by the new models and indicated an unreasonably deep value around 30-40 km. The inverted fault planes using the Love- and Rayleigh-wave structure shown by the thick-line in Figure 13a were not so different from the ones obtained above using the Love-wave structure (Table 9). The Rayleigh-wave velocity structure (the dashed-line in Fig. 13a) resulted in a rupture mechanism more like a reverse fault.

DISCUSSION AND RESULTS

The determination of the seismic moment tensor and the focal depth is one of the fundamental problems in seismology. The single-station approach using surface waves is one of the methods utilized in this context. Using both the synthetic and the actual records we have examined the performance of the method. We have shown that it works efficiently if one takes the necessary measures beforehand, otherwise it may result in highly unstable solutions.

The seismic velocity structure along the propagation path should be chosen reasonably correctly. Either former study in the region of interest or inversion of single-station group velocities could be used for this purpose. In the latter case, it is shown that the Love-wave group velocities are affected least by the source phase shift and result in most efficient velocity-depth profile that can be effectively used in the inversion of source characteristics. The Rayleigh-wave group velocities are affected most by the source phase shift when utilized at particularly small epicentral distances. This may lead to incorrect recovery of the propagation velocities and consequently cause instability in the solution. Error in the velocity structure primarily causes precision loss in the focal depth method.

It is shown that the use of relatively large wave-periods helps one alleviate the uncertainty due to the structural error. One should choose a minimum wave-period in a way that will minimize the effect of a possible error in the structure but also provide the desired precision in the solution. Multiple filter analysis in frequency-time domain can be used to extract this information directly from the recordings. The minimum wave-period obtained from particularly the Love-wave group velocities is adequate for this purpose. At the beginning, it is advantageous to start with a greater period value than what the recordings show. This initially gives a good sense of what the rupture mechanism and the focal depth approximately could be and then gradually smaller wave-periods in a few steps can be tested against possible increment in the precision of inversion. In addition, it is important that if a velocity structure obtained from a former study is used,

its validity should be checked with what frequency-time analysis of the specific event shows. This will keep one from starting with an error at the beginning.

The current method utilizes both amplitude and phase spectra of the recordings. The center of the source time function should be properly positioned along time axis in a way that will represent dominant moment release at the source. Possible dislocation of the presumed source time function as small as ± 2 - 3 s causes substantial mismatch in phase spectra that leads the method to break down. If the velocity structure is obtained directly from the recordings by assuming, for example, a unit-step dislocation pulse at the source, it should be centered at the origin time of event (i.e. 0 s). The source-pulse duration can be approximately adjusted by synthetic seismogram modeling. Particularly the higher-mode amplitudes are closely proportional to the pulse duration. As a final step, temporal match between synthetic seismograms and the actual records should be used to check the validity of the model parameters utilized in the inversion calculations. Particularly the large wave-periods of the two signals should match reasonably in both amplitude and arrival time.

ACKNOWLEDGMENTS

We would like to thank Prof. Costas Papazachos for his critical reviewing of the manuscript.

REFERENCES

Abo-Zena, A., 1979. Dispersion function computations for unlimited frequency values: Geophys. J. R. astr. Soc., **58**, 91-105.

Aki, K., and Richards, P.G., 1980. Quantitative seismology: Theory and methods: W.H. Freeman and Company, San Francisco, 259-333.

Anderson, D.L., 1989. Theory of the earth: Blackwell Scientific Publications, Brookline Village, MA, 45-62.

Ayele, A., and Arvidsson, R., 1998. Fault mechanisms and tectonic implication of the 1985-1987 earthquake sequence in south-western Ethiopia: J. Seismology, **1**, 383-394.

Chen, X., 1993. A systematic and efficient method of computing normal modes for multilayered half-space: Geophys. J. Int., **115**, 391-409.

Çakir, Ö., Erduran, M., Çinar, H., and Yilmaztürk, A., 2000a. Forward modeling receiver functions for crustal structure beneath station TBZ (Trabzon, Turkey): Geophys. J. Int., **140**, 341-356.

Çakir, Ö., Erduran, M., and Livaoglu, S., 2000b. The effect of the initial earthquake phase shift on the inversion of regional surface wave recordings for the estimation of crustal structure: Journal of the Balkan Geophysical Society, **3**, 20-36.

Di Bona, M., and Boatwright, J., 1991. Single-station decomposition of seismograms for subevent time histories: Geophys. J. Int., **105**, 103-117.

Dufumier, H., Michelini, A., Du, Z., Bondar, I., Sileny, J., Mao, W., Kravanja, S., and Panza, G.F., 1997. Regional structure modeling and source inversion for the 1992 Roermond earthquake: J. Seismology, **1**, 321-340.

Dziewonski, A.M., and Hales, A.L., 1972. Numerical analysis of dispersed seismic waves: in Methods in computational Physics: Bolt, B.A. (ed.), Academic Press, New York, **11**, 39-84.

Giardini, D., Boschi, E., and Palombo, B., 1993. Moment tensor inversion from mednet data (2) Regional earthquakes of the Mediterranean: Geophys. Res. Lett., **20**, 273-276.

Hartzell, S., Langer, C., and Mendoza, C., 1994. Rupture histories of eastern north American earthquakes: Bull. Seism. Soc. Am., **84**, 1703-1724.

Hermann, R.B., 1987. Computer programs in seismology, user's manual, vol. IV, St. Louis University, Missouri.

Jimenez, E., Cara, M., and Rouland, D., 1989. Focal mechanisms of moderate-size earthquakes from the analysis of single-station three-component surface-wave records: Bull. Seism. Soc. Am., **79**, 955-972.

Kausel, E.G., Schwab, F., and Mantovani, E., 1977. Oceanic Sa: Geophys. J. R. astr. Soc., **50**, 407-440.

Kennett, B.L.N., 1989. Lg-wave propagation in heterogeneous media: Bull. Seism. Soc. Am., **79**, 860-872.

Koch, K., and Stump, B., 1995. Implications for upper-mantle structure in the western United States from complete far-regional seismograms: Bull. Seism. Soc. Am., **85**, 1432-1444.

Lay, T., and Wallace, T.C., 1995. Modern global seismology: Academic Press. Inc., San Diego, 203-433.

Levshin, A.L., Ritzwoller, M.H., and Resovsky, J.S., 1999. Source effects on surface wave group travel times and group velocity maps: Phys. Earth Planet. Inter., **115**, 293-312.

Mantovani, E., Schwab, F., Liao, H., and Knopoff, L., 1977. Teleseismic Sn: a guided wave in the mantle: Geophys. J. R. astr. Soc., **51**, 709-726.

Mendiguren, J.A., 1977. Inversion of surface wave data in source mechanism studies: J. Geophys. Res., **82**, 889-894.

Mindevalli, Ö.Y., 1988. Crust and upper mantle structure of Turkey and the Indian sub-continent from surface wave studies: PhD thesis, Saint Louis University, 164 pages.

Papazachos, B., Kiratzi, A., and Papadimitriou, E., 1991. Regional focal mechanisms for earthquakes in the Aegean area: PAGEOPH, **136**, 405-420.

Shi, J., Kim, W.Y, and Richards, P.G., 1996. Variability of crustal attenuation in the northeastern United States from Lg waves: J. Geophys. Res., **101**, 25231-25242.

Sileny, J., Panza, G.F., and Campus, P., 1992. Waveform inversion for point source moment tensor retrieval with variable hypocentral depth and structural model: Geophys. J. Int., **109**, 259-274.

Takeuchi, H. and Saito, M., 1972. Seismic surface waves: in Methods in computational Physics: Bolt, B.A. (ed.), Academic Press, New York, **11**, 217-294.

Tarantola, A., 1987. The least-squares criterion: in Inverse problem theory: Elsevier Science Company Inc., New York, 187-255.

Panza, G.F., Sileny, J., Campus, P., Nicolich, R., and Ranieri, G., 1993. Point source moment tensor retrieval in volcanic, geothermal and orogenic areas by complete waveform inversion: J. Appl. Geophys., **30**, 89-118.

Taymaz, T., Eyidogan, H., and Jackson, J., 1991. Source parameters of large earthquakes in the east Anatolian fault zone (Turkey): Geophys. J. Int., **106**, 537-550.

Yilmaztürk, A., Bayrak, Y., and Çakir, Ö., 1999. Crustal seismicity in and around Turkey: Natural Hazards, **18**, 253-267.